Available online at www.sciencedirect.com
ScienceDirect
International Journal of Heat and Mass Transfer 51 (2008) 4829–4840
International Journal of HEAT and MASS TRANSFER
www.elsevier.com/locate/ijhmt

Numerical comparison of thermoacoustic couples with modified stack plate edges

L. Zoontjens *, C.Q. Howard, A.C. Zander, B.S. Cazzolato

School of Mechanical Engineering, The University of Adelaide, South Australia 5005, Australia

Received 25 July 2007; received in revised form 16 February 2008
Available online 9 May 2008

Abstract

It has been demonstrated that the bulk of time-averaged heat transfer between the oscillating fluid and a thermoacoustic couple is concentrated towards the edges of the stack plate. Previous numerical studies which have considered thermoacoustic couples of finite thickness have used a rectangular form for the plate edge. In practice however, current manufacturing practices allow for a variety of stack edges which may improve the efficiency of heat transfer and/or reduce entropic losses. In this numerical study, the performance of a thermoacoustic couple is investigated at selected drive ratios and using a variety of stack plate edge profiles. Results indicate that stack profiles with enlarged and blunter shapes improve the rate of heat transfer at low drive ratios but retard the rate of heat transfer at higher drive ratios due to increased residence time of the fluid in contact with the stack plate. The improvement in COP through minimisation of acoustic streaming on the inside face of the stack, and increased effective cooling power by greater retention of stack thickness at the plate extremities, leads to recommendation of the Rounded edge shape profile for thermoacoustic stack plates in practical devices.

Keywords: Thermoacoustics; Heat; Sound; Thermoacoustic couples; Heat exchangers; Acoustic streaming

1. Introduction

Thermoacoustic devices can potentially use high-amplitude sound waves to serve a variety of purposes in fields such as cryogenics, cost-effective domestic refrigeration or electricity generation, without drawbacks such as expensive construction or maintenance costs, high part counts or adverse environmental impact associated with certain refrigerators. With greater media and scientific interest in the issues of climate change, thermoacoustics is also an increasingly popular field of study because of its potential advantages over conventional systems.

The thermoacoustic stack is considered to represent the 'heart' of practical thermoacoustic devices since it is the location at which effective conversion of energy occurs [1, Section 1.3.1] and is usually the starting point for system design. The stack (or core) presents a series of small gas channels in intimate contact with the working fluid, and is conventionally formed as a series of parallel plates at a fixed pitch, although other construction configurations are commonly used, such as the rectangular cell sections used in ceramic substrates in automotive catalytic converters.

'Linear theory', which collectively refers to quantitative one-dimensional thermoacoustic prediction tools and formulations in development over the last 30 years [1–4], has developed to the point where effective design and optimisation of thermoacoustic devices operating *at low pressure amplitudes* can be made. However, high pressure amplitude operation of thermoacoustic devices has been shown to deviate significantly from linear theory predictions.

The vast proportion of two-dimensional numerical studies specific to thermoacoustic devices in the literature have modelled what Wheatley et al. [5] termed a 'thermoacoustic

* Corresponding author. Tel.: +61 8 8303 5460.
E-mail address: luke.zoontjens@alumni.adelaide.edu.au (L. Zoontjens).

0017-9310/$ - see front matter © 2008 Elsevier Ltd. All rights reserved.
doi:10.1016/j.ijheatmasstransfer.2008.02.037

Nomenclature

a	gas sound speed, m/s
A	cross-sectional area, m^2
BR	blockage ratio
c_p	gas heat capacity, J/kg K
c_{ps}	plate material heat capacity, J/kg K
DR	drive ratio
$\dot{E}_2$	time-averaged acoustic power, W
f	frequency, Hz
$\langle \dot{h}_{hx} \rangle_t$	time-average heat flux over heat exchanger boundary, W/m^2
$\langle \dot{h}_x \rangle_t$	time-average heat flux in the x direction, W/m^2
$\langle \dot{h}_y \rangle_t$	time-average heat flux in the y direction, W/m^2
k	gas wavenumber, m^{-1}
k_s	plate thermal conductivity, W/mK
k_0	gas thermal conductivity, W/mK
L_A	axial length of subdomain 'A', m
L_B	axial length of subdomain 'B', m
L_{CV}	axial length of control volume, m
L_S	stack plate length, m
n_x	number of mesh grid intervals along edge in x direction
n_y	number of mesh grid intervals along edge in y direction
p_A	pressure amplitude at pressure antinode, Pa
p_m	mean operating pressure, Pa
$\lvert p_1 \rvert$	first-order acoustic pressure amplitude, Pa
Pr	Prandtl number
$\dot{Q}$	time-averaged thermal power, W
S	heat exchanger surface
t	time, s
t_s	stack plate half-thickness, m
T_k	gas temperature, K
T_0	initial gas temperature, K
u	x component of velocity, m/s
$\lvert u_1 \rvert$	first-order acoustic velocity amplitude, m/s
v	y component of velocity, m/s
$\lvert U_1 \rvert$	first-order volumetric flow rate amplitude, m^3/s
x	axial co-ordinate/dimension, m
x'	axial distance from centre of resonator, m
y	transverse co-ordinate/dimension, m
y_0	stack plate half-spacing, m

Greek symbols

γ	ratio of specific heats
δ_κ	thermal penetration depth, m
$\delta_{\kappa m}$	mean thermal penetration depth, m
δ_v	viscous penetration depth, m
$\Delta T_{k,hx}$	axial gas temperature difference across heat exchanger, K
Δx	mesh interval spacing in x direction, m
Δy	mesh interval spacing in y direction, m
λ	wavelength, m
ρ	density, kg/m^3
ω	angular frequency ($=2\pi f$), rad/s
μ	dynamic viscosity, kg/ms
ρ_s	density of the stack material, kg/m^3
υ	kinematic viscosity, m^2/s

couple' (TAC), which in its most abstract form is a single infinitely wide plate in an oscillatory flow field. Presumably, the thermoacoustic couple is intended to provide a tractable means to approximate a stack consisting of many parallel plates.

In one of the first two-dimensional numerical studies of thermoacoustic couples, Cao et al. [6] found that the time-averaged rate of heat transfer across the plate was concentrated at the edges. Mozurkewich [7] later confirmed this result using an analytical boundary value approach, noting that the area over which the time-averaged heat transfer is concentrated is of similar order to the gas displacement amplitude. The time-averaged rate of heat transfer across the boundary of the thermoacoustic couple is of significant interest in numerical studies, because it is an effective performance measure which allows comparison between stack plates of varying geometry and location in the acoustic field.

Previous studies have considered the effect of finite plate thickness upon the rate of heat and flow transportation pertaining to the thermoacoustic couple or stack plate [8,9]. The stack plate was represented by a rectangular section; however in practice, typical parallel plate or spiral stacks do not have perfectly square leading edges, and modern manufacturing techniques permit the design and construction of profiled edges. With existing literature considering only rectangular or zero-thickness (1-D) plates, it would be interesting to see if performance gains could be achieved using non-rectangular cross sections, such as those with rounded or elliptically shaped plate edges.

Section 2.1 presents the variants of edge shape considered in this study, and a brief discussion of the modelspace and parameters used. The performance of each plate edge shape variant is compared using the measures defined in Section 2.6. Results using these performance measures are presented in Section 3 and are discussed in Section 4.

2. Numerical model

For the sake of comparison with previous studies [6,10,11], the numerical model employed in this study uses similar operating conditions but an expanded solution domain to account for physical flow disturbances. The simulation parameters and implementation of the numerical model is otherwise consistent with these studies. The model approximates a closed-ended, half-wavelength standing wave resonator duct filled with helium at 10 kPa absolute

pressure, with a parallel-plate stack located in one end of the device. As the resonator length is fixed at 5.04 m and the sound speed of the gas at ambient temperature $T_0 = 300$ K is $a = 1008$ m/s, the operating frequency of the device is fixed to have the first natural frequency at 100 Hz.

Fig. 1 presents a computational domain in the context of the theoretical half-wavelength resonator. The resonator is shown as a two-dimensional representation of a smooth duct with rigid terminations at each end. Ignoring the effects of the resonator diameter and duct surfaces, a parallel-plate stack located inside the resonator is considered to be of infinite width and plate count for the purposes of this study.

2.1. Modelspace

The modelspaces used to investigate the effect of different plate end shapes were adapted from a model used for non-zero-thickness stack plates [12] and are shown in Fig. 2. For all shapes considered, the overall plate length of $L_S = 0.252$ m and the plate half-thickness t_s at mid-length of 2.4 mm were kept constant, to enable comparison with the results of previous studies [12] and to maintain plate spacing and length scales consistent with the numerical study of Ishikawa and Mee [10]. The edge shapes considered in this study are as follows:

(i) *Rectangular* (Fig. 2b): Stack plates which are truly rectangular in cross section serve as a good benchmark especially for comparison with zero-thickness stack plates (Fig. 2a).

(ii) *Rounded edges* (Fig. 2c): Fillets with radius equal to the plate half-thickness t_s are applied to the rectangular stack shape. The elimination of the right-angled edges is anticipated to reduce the flow impedance and flow recirculation near the plate extremities. Rounded edge stack plates could potentially be manufactured using abrasive techniques.

(iii) *Bulbous edges* (Fig. 2d): Semi-circular sections with radius equal to twice the plate half-thickness t_s are centred $2t_s$ inside each end of the plate. The increased flow impedance at the plate extremities might improve the performance of the stack by 'constraining' fluid parcels within the stack region. In practice a bulbous section could potentially be manufactured by dipping a stack into an adhesive or molten material which would then be allowed to harden into the bulbous edge shape.

(iv) *Talon edges* (Fig. 2e): Circular quadrants with radius $2t_s$ are centred $2t_s$ inside each end of the plate and located such that the chord of each quadrant faces outward from the stack interior. Between the two quadrants is a plate of thickness t_s. This edge shape design was considered as a means to further constrain fluid within the stack region. Larger stacks could potentially incorporate this plate edge shape by attaching suitably shaped tips.

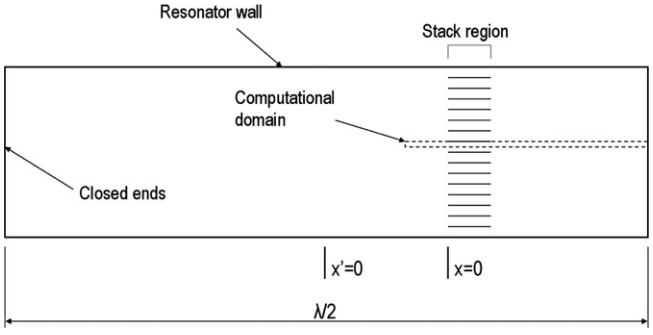

Fig. 1. Locus of the computational domain within the basic theoretical model of a half-wavelength resonator tube with parallel-plate stack. Acoustic source not shown.

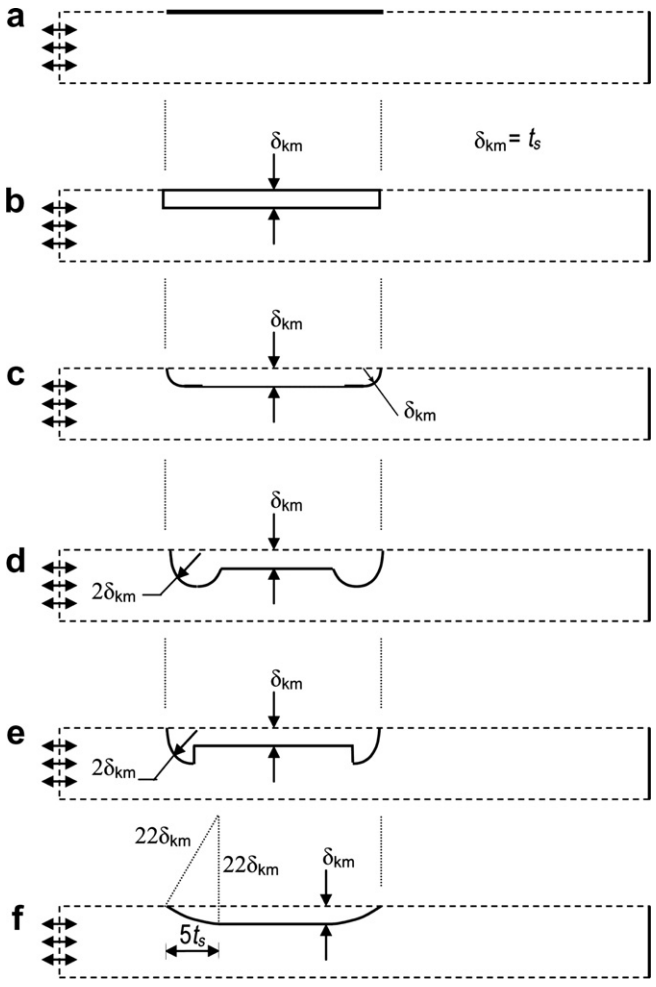

Fig. 2. Sketches of modelspaces used for modelling different stack plate end shapes: (a) zero-thickness plates [6,10], (b) Rectangular (finite thickness), (c) Rounded edges, (d) Bulbous edges, (e) Talon edges and (f) Aerofoil edges. All modelspaces shown are otherwise identical to that presented in Fig. 4. As indicated, the plate half-thickness t_s in the centre of the stack region is equal to the mean thermal penetration depth δ_{km}. The vertical dotted lines indicate that each plate edge is located at the same axial position in the resonator.

(v) *Aerofoil edges* (Fig. 2f): Aerofoil tips with a foil chord length arbitrarily set to $5t_s$ (i.e. an aspect ratio of 5) are added to each end of the plate stack. The edge is implemented in the modelspace using the chord of a circle $22t_s$ in diameter. Minimising the flow impedance presented may result in increased movement of the fluid parcels and transfer of heat down the length of the stack. Aerofoil stack plates for larger thermoacoustic systems could potentially be manufactured with minimal effort using die-forming or injection-moulding systems.

The modelspace used for the current work is divided into six subdomains which together can facilitate changes to the fundamental characteristics of the thermoacoustic environment, such as the variation of plate thickness or duct length. Fig. 3 shows a sketch of the modelspace used in this study.

The plate and thermal reservoir comprises subdomains 'P' and 'H', respectively. Subdomain 'S' is the region encompassed by the plate axially within the stack. The length y_0 is the half-spacing between plate centrelines. Subdomains 'A' and 'B' enable consideration of flow structures which may develop outside the stack region due to non-zero plate thickness, and are of sufficient lengths L_A and L_B such that the pressure changes can be considered adiabatic. Subdomain 'C' links subdomain 'B' to the hard walled end of the duct located at the right edge of subdomain 'C'. Symmetric boundary conditions have been imposed on all lateral fluid boundaries, and an oscillatory boundary condition on the left side of subdomain 'A' has been used to represent an acoustic standing wave.

The inclusion of subdomain 'H' allows plates of zero thickness with finite heat capacity and thermal conductivity to be modelled, and although no plates of zero thickness are modelled in this study, this enables comparison with previous work. The thickness and hence influence of subdomain 'H' is intended to be minimal compared to that of subdomain 'P'. In following Piccolo and Pistone [11], the top and sides of subdomain 'H' are thermally insulated, forcing any excess heat entering regions 'H' and 'P' to return back through the boundaries between subdomain 'P' and subdomains 'A', 'S' and 'B'. The thermal properties of the stack are important because unsteady temperature distributions are allowed to form within the stack region. The shape of region 'P' is modified in the current study to model variants of stack plate edges.

Using the commercial code FLUENT, a two-dimensional, segregated and second-order implicit numerical model was developed which solves equations for continuity of mass, momentum and energy. The investigation utilises second order, double-precision discretisation of state variables and a laminar viscous model which relies on good near-wall resolution for effective modelling of the heat transfer rate.

2.2. Boundary conditions

Fig. 4a and b indicate the boundary types and various length scales used in this study. The conditions imposed upon the boundaries shown in Fig. 4a and b are described by Eqs. (1)–(5) with u and v the components of velocity in the x and y directions, and x' being the axial distance from the centre of the duct.

$$\left.\begin{aligned} u &= 0 \\ v &= 0 \\ \tfrac{dT}{dy} &= 0 \end{aligned}\right\} \text{ on axial 'WALL' boundaries,} \tag{1}$$

$$\left.\begin{aligned} u &= 0 \\ v &= 0 \\ \tfrac{dT}{dx} &= 0 \end{aligned}\right\} \text{ on transverse 'WALL' boundaries,} \tag{2}$$

$$\left.\begin{aligned} u &= 0 \\ v &= 0 \end{aligned}\right\} \text{ on 'HX' boundaries,} \tag{3}$$

$$\left.\begin{aligned} v &= 0 \\ \tfrac{dT}{dy} &= 0 \end{aligned}\right\} \text{ on 'SYM' boundaries, and} \tag{4}$$

$$p = p_m + Re\left[|p_1|e^{j(\omega t + kx' - \frac{\pi}{2})}\right] \text{ on 'INLET' boundaries.} \tag{5}$$

The axial length of subdomains 'A' and 'B' were set equal to $L_A = L_B = 0.15$ m. The axial length of the computational domain, L_{CV}, was set to 1.476 m. As shown in Fig. 1, the origin of the computational domain is located 1.194 m axially from the centre of the duct, i.e. $x' = x + 1.194$ m.

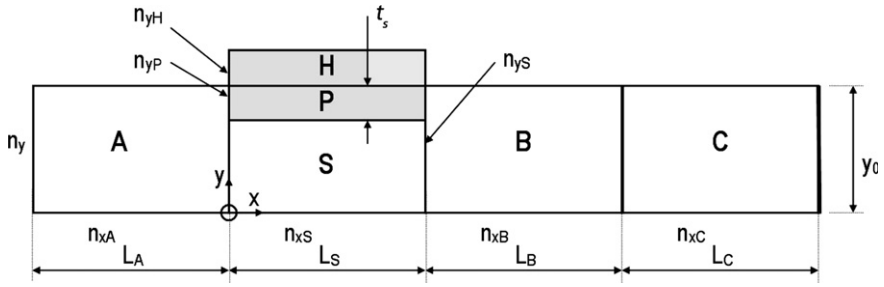

Fig. 3. Annotated sketch of the basic thermoacoustic couple modelspace. Shaded areas are regions of solid material and unshaded areas are fluid regions. The half-thickness of the plate is modelled using finite t_s, and appropriate selection of the number of mesh intervals in the x and y directions, $n_{xP}(= n_{xS})$ and n_{yP}.

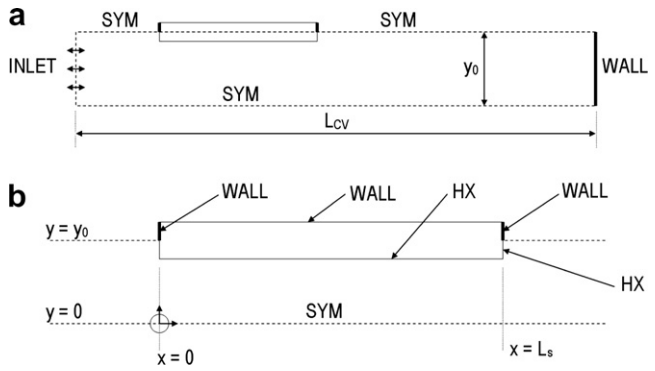

Fig. 4. Computational domains used in this study showing boundary conditions and selected geometry; (b) provides a closer view of the stack region shown in (a).

Fig. 4 indicates the boundary conditions used in each simulation. Stack periodicity is assumed in the transverse direction and the model extends to a rigid end wall.

For each run, a sinusoidal pressure input applied to the inlet boundary shown in Fig. 4(a) with frequency $f = 100$ Hz and amplitude $|p_1|$ as listed in Table 1. In transient or unsteady thermoacoustics, a key term used is the 'limit state' or 'limit cycle', which refers to the state of operation or operating conditions in which the phase and magnitude of state variables such as p, U and T at each phase in the cycle do not vary from one oscillation to the next. In the context of numerical modelling thermoacoustic couples, the 'limit state' is not equivalent to an experimental sense, where the limit state is usually observed from stabilisation of measured temperature differences (with orders-of-magnitude larger time constants). Here, the simulation is advanced in time until pressure, velocity and performance measures such as $\Delta T_{k,hx}$ and $\langle \dot{h}_{hx} \rangle_t$ stabilise to within computational error on a cycle to cycle basis.

To ensure each simulation achieved limit state operation, two thousand time steps (20 oscillations) were calculated to initialise each model. An additional 100 time steps (1 full cycle) was then simulated with statistical averaging employed to determine properties such as the time-averaged heat flux distribution or flow parameter.

2.3. Operating conditions

Table 1 presents the operating conditions for each run considered in this study. To investigate the influence of stack plate edge shape, each of the modelspaces shown in Fig. 2 are compared for identical global operating conditions and increasing drive ratio DR. Runs 11–20 use a drive ratio above 3% to provoke a siginificant increase in non-linear effects associated with the flow impedance of each edge shape. For all runs, $t_s = \delta_{\kappa m} = 0.024$ m in the plate midsection which leads to a blockage ratio BR ($= 1 - t_s/y_0$) of 0.7.

Table 1
Run number for stack plate edge shape and drive ratio

Edge shape (Fig. 2)	$\lvert p_1 \rvert / p_m$(%)			
	1.7	3.4	5.1	6.8
Rectangular	1	6	11	16
Rounded	2	7	12	17
Bulbous	3	8	13	18
Talon	4	9	14	19
Aerofoil	5	10	15	20

For all runs, $t_s = \delta_{\kappa m} = 0.024$ m, $BR = 0.7$ at plate mid-length.

2.4. Material properties

Table 2 lists the physical properties used in each simulation. For comparison with results obtained in previous studies, consistent material properties and acoustic conditions are retained. Use of helium at ~10% atmospheric pressure as the working fluid also enables comparison with the results of Ishikawa and Mee [10], albeit for the zero-thickness stack plate used in their work. The temperature dependence of gas thermal conductivity k_0 and dynamic viscosity μ are modelled using a linear piecewise approximation based upon published values according to temperature [14].

The density of the solid material is set lower than that expected in practical devices, to exaggerate any internal temperature differentials obtained in the study, whilst maintaining a thermal capacity significantly higher than that of the oscillating gas.

2.5. Numerical implementation

The meshes used in this study are summarised in Table 3. The circular and curved elements present in many of the modelspaces was achieved by applying triangular and quadrilateral mesh elements using default 'PAVE' settings within the *GAMBIT* (v2.3.16) environment. Consistent mesh spacings along subdomain boundaries were retained for all models considered in this study.

Non-rectangular quad elements were used to model curved plate edges and nodes were concentrated to the plate edges and heat exchange surfaces. A ratio of $\delta_\kappa/\Delta y = 60$ achieved for the Rectangular model is at least matched or exceeded for the other models studied.

2.6. Performance measures

The influence of the stack plate edge shape will be assessed using the performance metrics discussed in the following subsections.

2.6.1. Heat transfer

The distribution of time-averaged heat flux density over an oscillatory cycle at a fluid–solid boundary, $\dot{h}$, is a useful performance measure that has been used in the majority of past studies of thermoacoustic couples. In previous studies which considered a stack plate of zero thickness [6,10,11], this quantity was also referred to as a time-average heat flux in the transverse or y-direction, which is here

Table 2
Flow conditions and material properties used for all runs

Property	Value	Units
Operating frequency, f	100	Hz
Ambient temperature, T_0	300	K
Mean pressure, p_m	10	kPa
Gas properties		
Prandtl number, Pr	0.69	
Heat capacity, c_p	5,193	J/kg K
Thermal conductivity, k_0	Piece-wise linear approx. [14, Table A-7]	
Dynamic viscosity, μ	Piece-wise linear approx. [14, Table A-7]	
Ratio of specific heats, γ	1.665	
Plate material properties		
Thermal conductivity, k_s	10	W/m K
Heat capacity, c_{ps}	400	J/kg K
Density, ρ_s	400	kg/m^3

Table 3
Grid mesh data for each modelspace used in this study

Edge Profile	Node count		n_{xS}	n_y	Typ. $\delta_\kappa/\Delta y$	e_{xA}, e_{xB}
Rectangular	159,418	}	504	200	$\geqslant 60$	1.0
Rounded	131,217					
Bulbous	151,579					
Talon	150,780					
Aerofoil	139,643					

Here, $\delta_\kappa/\Delta y$ is the minimum ratio of thermal penetration depth to grid mesh spacing normal to and within δ_κ of the heat exchanger surface. n represents the number of grid intervals in specified direction and subdomain. e is the exponential ratio used within *GAMBIT* [13] to grade the mesh along each subdomain boundary.

represented by $\langle \dot{h}_y \rangle_t$. The term $\langle \dot{h}_{hx} \rangle_t$ will refer to the time-average heat flux through all fluid–solid boundaries of the stack plate and includes heat transfer in the axial direction, $\langle \dot{h}_x \rangle_t$.

In this study, where the heat exchanging surfaces of the stack plate are not orthogonal, it is important to define the heat flux through the plate surface using vectors normal to the heat exchanger surface S as shown in Fig. 5.

The integral of heat flux $\dot{h}$ through the plate surface S is therefore defined by

$$\dot{h}_{hx} = \dot{h}_S = \int_S \dot{h} \cdot \mathbf{n} \, \mathrm{d}A \tag{6}$$

and represents the magnitude of heat flux via the plate surface. However, this value can be misleading as it combines

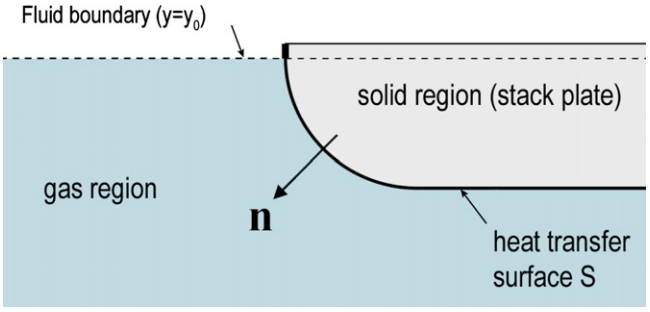

Fig. 5. Example normal vector **n** to the heat exchanger surface S.

negative heat flux (i.e. cooling of the plate) as well as positive heat flux. Conservation of energy requires that for a domain of constant temperature that is fully insulated and/or enclosed by surface S, the sum of heat flux ($\dot{h}$) over the surface S is zero. In practice though, the internal temperature of the stack plate varies within the plate despite all surfaces at solid–fluid boundaries being fixed at 300 K. Entropic losses are also included in the model and are expected to create minor additional heat flux which is included in the integral of Eq. (6).

An improved method is to treat the stack region as comprising only two surface groups: a 'cold' surface in which the time-averaged heat flux is negative, and a 'hot' surface for which the time-averaged heat flux is positive. A point on the surface S at which the time-averaged heat flux at limit state is zero is used to divide the stack plate into 'cold' and 'hot' ends or regions. Fig. (6) illustrates this method for an arbitrary thermoacoustic couple plate surface. As indicated in this figure, the 'cold end' corresponds to the section of plate for which $\langle \dot{h} \rangle_t < 0$ at the solid–fluid boundary, and its axial length is denoted by $L_{S,cold}$. Similarly for $\langle \dot{h} \rangle_t > 0$ on S at the 'hot end' spanning $L_{S,hot}$ where $L_s = L_{S,cold} + L_{S,hot}$. The surfaces on S for which $\langle \dot{h} \rangle_t < 0$ and $\langle \dot{h} \rangle_t > 0$ are denoted by S_{cold} and S_{hot}, respectively. For more complex surfaces, S_{cold} and S_{hot} may not be continuous, as will be shown for the Talon edge model in Section 3.1.

As shown in Fig. 6, this approach sets the boundary between the 'cold' and 'hot' ends of the plate as being straight and perpendicular to the predominant flow vector. In practice, this boundary may be distorted from a straight line.

The performance measure considered here is therefore the total time averaged thermal power transferred from the cold section of the plate per unit width, or

$$\dot{Q}_{S,cold} = \int_{S_{cold}} \dot{h} \cdot \mathbf{n} \, \mathrm{d}A. \tag{7}$$

2.6.2. Temperature differentials

A measure of the time-average difference in area-weighted average gas temperature at $x = 0$ and $x = 0.252$ m is given by $\Delta T_{k,hx}$, and can be considered the axial gas temperature difference across the heat exchanging surface, hence the subscript 'hx', where

$$\Delta T_{k,hx} = \langle (|T_k|_{x=0.252\ \mathrm{m}} - |T_k|_{x=0}) \rangle_t. \tag{8}$$

Experimental studies of thermoacoustic couples often cite the 'edge-to-edge' temperature difference as a performance metric [5] and $\Delta T_{k,hx}$ is here considered to be its numerical equivalent.

2.6.3. Acoustic power input to the system

The scaling of performance measures such as $\Delta T_{k,hx}$ and $\dot{Q}_{S,cold}$ is normalised by the time-averaged acoustic power $\dot{E}_2$ input to the system.

Considering that all solid external boundaries to the thermoacoustic couple model are thermally insulated, it

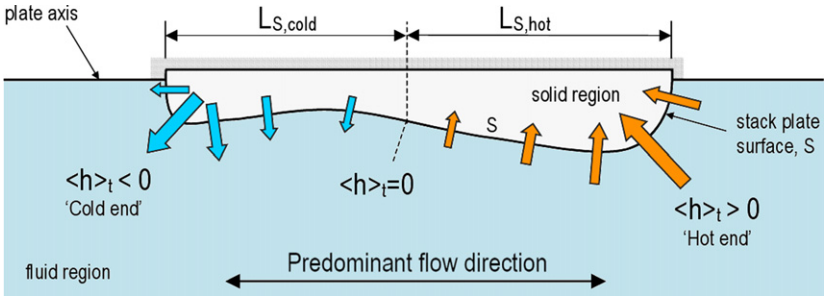

Fig. 6. Diagram of a thermoacoustic couple with arbitrarily shaped heat exchanger surface S.

follows that the time-averaged net acoustic power absorbed by the system is equal to $\dot{E}_2$ on the inlet boundary. In this study This single inlet to the domain comprises 100 face elements and is of sufficient proximity to the stack region for the velocity field to contain significant transverse velocity components.

On the inlet boundary shown in Fig. 7, the pressure is set to

$$p|_{\mathrm{INLET}} = |p_1|\sin(kx')\sin(\omega t) \tag{9}$$

and 1-D volume velocity response at limit state is therefore

$$U|_{\mathrm{INLET}} = |U_1|\cos(\omega t + \phi_{pU}), \tag{10}$$

where x' is the distance to the centre of the model, as shown in Fig. 1, such that the term sin (kx') is used to achieve $|p_1|$ at the resonator terminations. ϕ_{pU} represents the phase angle between pressure and volume velocity.

With this information, $\dot{E}_2$ is defined by [1, Eq. (5.3)]

$$\dot{E}_2 = \frac{1}{2}Re\{p_1 U_1^*\} = \frac{1}{2}Re\{p_1^* U_1\}, \tag{11}$$

where the asterisk $(*)$ indicates complex conjugate, or [1, Eq. (5.4)]

$$\dot{E}_2 = \frac{1}{2}|p_1||U_1|\cos\phi_{pU}. \tag{12}$$

However, pressure and velocity data is real within the *FLUENT* environment and it is therefore difficult to estimate $\dot{E}_2$ based upon Eqs. (11) or (12). Applying Eq. (10) using curve-fitting techniques to determine the phase angle ϕ_{pU} are difficult with transverse velocity components on INLET. However, by assuming the time-average axial position of fluid along the boundary to coincide with the boundary itself, the acoustic power is estimated using [1, Eq. (5.6)]

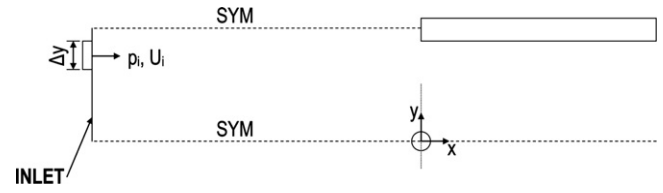

Fig. 7. Sketch describing the determination of acoustic power $\dot{E}_2$ within the *FLUENT* CFD environment, using pressure p_i and volume velocity U_i obtained at the ith segment of boundary 'INLET'.

$$\dot{E}_2 = \frac{\omega}{2\pi}\oint pU\,\mathrm{d}t \tag{13}$$

or with fixed time step size and Δy on the inlet boundary,

$$\dot{E}_2 = f\int\int_{\mathrm{INLET}} pU\,\mathrm{d}y\,\mathrm{d}t, \tag{14}$$

which can be obtained from the *FLUENT* environment using a custom field function.

Although the pressure amplitude and hence drive ratio is set equal in each model, the difference in acoustic velocity fields will require that $\dot{E}_2$ be used to normalise the results obtained.

2.6.4. Coefficient of performance

The coefficient of performance of the thermoacoustic couple is defined here as

$$\mathrm{COP} = \frac{\dot{Q}_{\mathrm{S,cold}}}{\dot{E}_2} \tag{15}$$

with $\dot{E}_2$ representing the time-average acoustic power input to the system, as calculated using Eq. (14).

3. Results

In the following subsections each edge shape will be compared on the basis of effective heat transfer, cooling power, temperature distribution and overall efficiency.

3.1. Heat transportation

Fig. 8 presents the integral of the time averaged heat flux normalised by the result obtained using the Rectangular edge shape, versus the ratio of acoustic power input $\dot{E}_2$, normalised by the result of Run 1. At a drive ratio of 1.7%, where $\dot{E}_2/\dot{E}_2|_{\mathrm{Run\ 1}} \approx 1$, all four alternative stack plate edge shapes achieve a higher rate of heat transfer in comparison to the rectangular shape section. However, at a drive ratio of 6.8%, the Talon, Bulbous and Aerofoil edge shapes underperform despite higher acoustic power inputs.

The rounded edge shape performs noticeably differently from the other edge shapes considered in that it is more effective than the Rectangular edge shape for all drive ratios modelled. It was expected that this result would also be achieved using the Aerofoil edge shape, since both the

Aerofoil and Rounded edge shapes present curved edges to reduce flow impedance. However, Fig. 8 suggests that this is only true for a low pressure amplitude, with the Aerofoil edge shape result deviating from the Rounded edge shape result at drive ratios of 5.1% and 6.8%.

The time-averaged heat flux is plotted using drive ratios of 1.7% and 6.8% for all stack plate edge shapes considered in Figs. 9 and 10, respectively, which reveal a dramatic difference in $\langle \dot{h}_{hx} \rangle_t$ obtained using the Bulbous and Talon edged shapes with vertical 'spikes' in the time-averaged heat flux inside the stack region. The corner intersection or crevice on the inside of the stack region is a location of poor effective heat transfer, and when considered over a full period, its impact is counter-productive to the thermoacoustic effect desired. This effect demonstrated using the Bulbous edge shape is exaggerated by the Talon edge shape. Figs. 11 and 12 show this in closer detail of the left ('cold') end of the stack plate. Despite this effect occurring at all the drive ratios simulated, the overall value of $\langle \dot{h}_{hx} \rangle_t$ is shown in Fig. 8 to be highest for the Talon and Bulbous edge shapes at a DR of 1.7%.

Whilst Fig. 8 shows the Bulbous and Talon edge shapes to be more effective in increasing the total rate of effective heat transfer at a DR of 1.7%, Figs. 9–12 show ineffective or adverse performance (marked with *) near the 'crevice' of the edge feature inside the stack region. At a drive ratio of 1.7%, the Bulbous and Talon edge shapes are shown in Fig. 11 to result in a smaller magnitude of $\langle \dot{h}_{hx} \rangle_t$ over the inside 3–10% of stack length. This deficiency is larger at higher drive ratios, as shown in Figs. 10 and 12, although the stack length over which this deficiency is evident is significantly larger on the cold side of the stack than on the hot side.

Figs. 9 and 11 show that over each outer 10% of the stack plate length, the Rounded and Aerofoil edge shapes are shown to induce greater $\langle \dot{h} \rangle_t$ than the Rectangular edge shape. At other stack locations, these three edge shapes are shown to achieve near identical values of $\langle \dot{h} \rangle_t$. However according to Fig. 8, the Bulbous and Talon plate edge shapes achieve a higher total time-averaged heat flux at a drive ratio of 1.7%. This is because these two stack plate edge shapes have a greater surface area at the edges where the rate of heat transfer is concentrated, and the flow disturbance due to the greater surface area is not excessive.

Figs. 13 and 14 show the relative distribution of $\langle \dot{h} \rangle_t$ over the Talon edge surface for drive ratios of 1.7% (Run 4) and 6.8% (Run 19), respectively. These two figures show that as the drive ratio is increased, the distribution of effective heat transfer shifts to the tip of the protruding edge. The distribution of $\langle \dot{h} \rangle_t$ is noticeably more perturbed on the rounded leading edge. As discussed previously and indicated (*) in Figs. 11 and 12 at $x/L_S \approx 0.019$, $\langle \dot{h} \rangle_t$ is positive in the 'crevice'. The Bulbous edge shape which also features a large protusion at the stack plate edge, also results

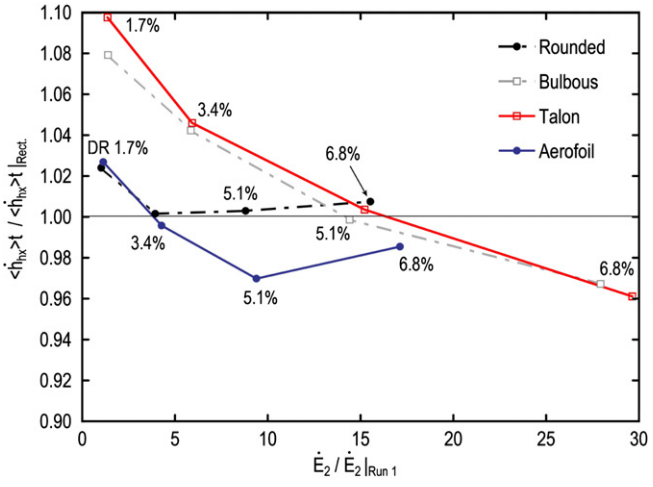

Fig. 8. $\langle \dot{h}_{hx} \rangle_t$ (normalised using rectangular edge shape result) versus $\dot{E}_2$ normalised by the result of Run 1. Four points of increasing *DR* (labelled left to right) are plotted for each edge shape.

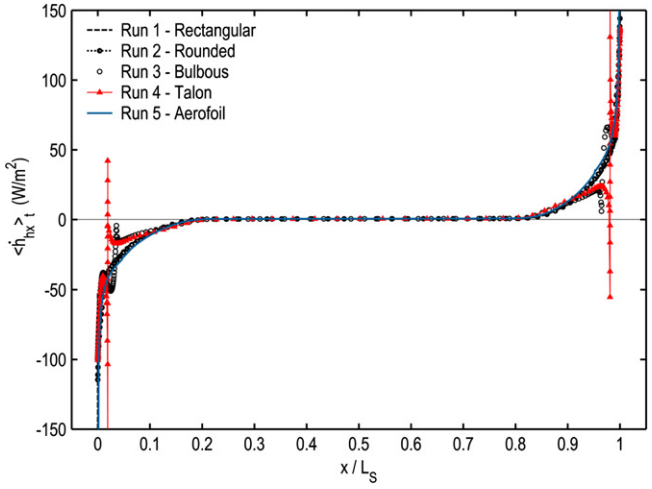

Fig. 9. Distribution of time-averaged heat flux across the heat exchanger surface $\langle \dot{h} \rangle_t$ with normalised axial position x/L_S for a drive ratio of 1.7% (Runs 1–5).

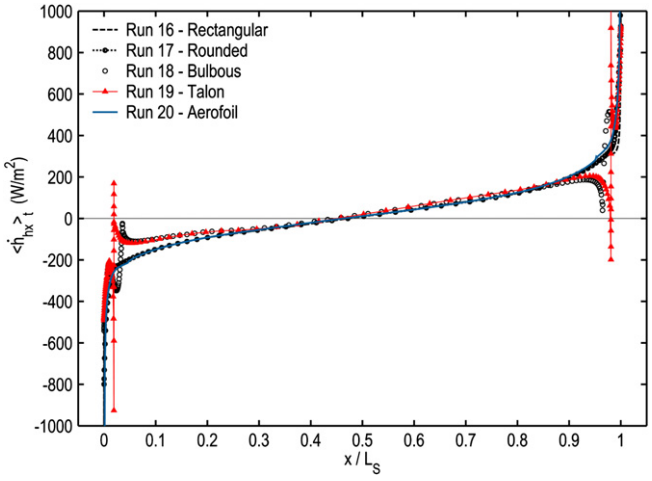

Fig. 10. Distribution of time-averaged heat flux across the heat exchanger surface $\langle \dot{h} \rangle_t$ with normalised axial position x/L_S for a drive ratio of 6.8% (Runs 16–20).

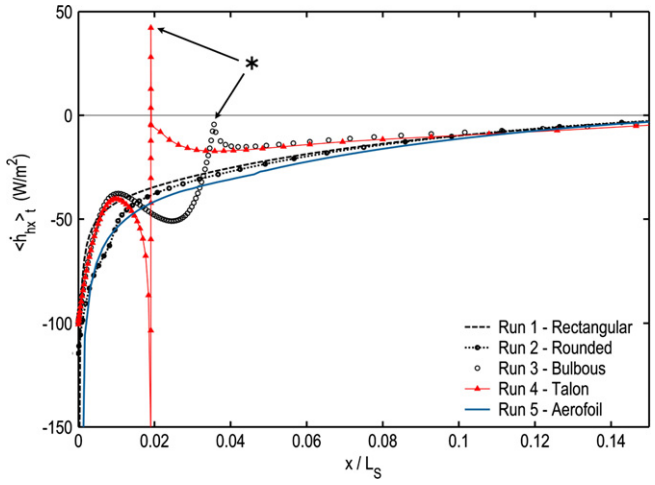

Fig. 11. Distribution of time-averaged heat flux across the heat exchanger surface $\langle \dot{h} \rangle_t$ with normalised axial position x/L_S for a drive ratio of 1.7% showing increased detail near the 'cold' end of the thermoacoustic couple. Runs 1–5 shown (DR of 1.7%). Distortions in $\langle \dot{h} \rangle_t$ due to sudden bends in the shapes of the Talon and Bulbous edge profiles are highlighted (*).

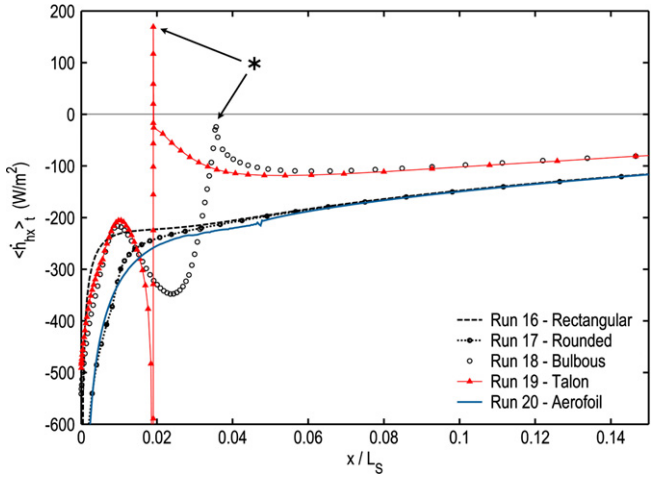

Fig. 12. Distribution of time-averaged heat flux across the heat exchanger surface $\langle \dot{h} \rangle_t$ with normalised axial position x/L_S for a drive ratio of 6.8% showing increased detail near the 'cold' end of the thermoacoustic couple. Runs 16–20 shown (DR of 6.8%). Distortions in $\langle \dot{h} \rangle_t$ due to sudden bends in the shapes of the Talon and Bulbous edge profiles are highlighted (*).

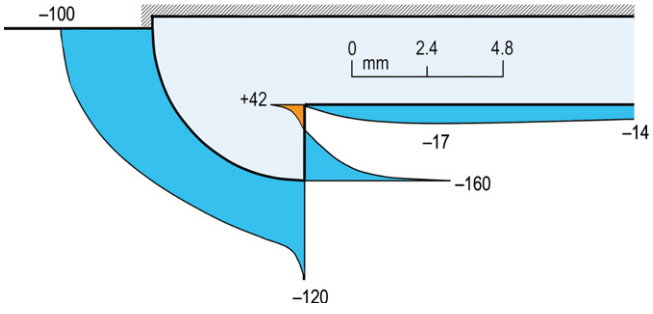

Fig. 13. Time-averaged heat flux $\langle \dot{h} \rangle_t$ across the cold end of the Talon edge (Run 4). Drive ratio is 1.7%.

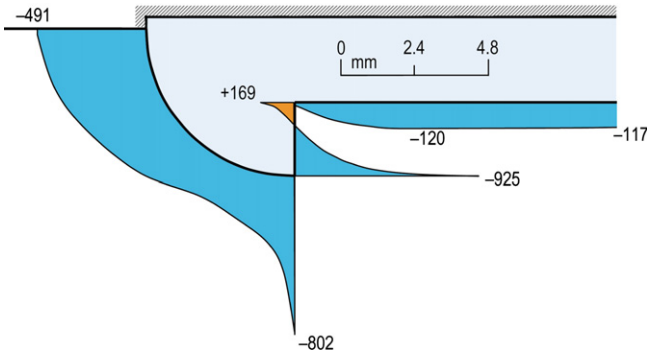

Fig. 14. Time-averaged heat flux $\langle \dot{h} \rangle_t$ across the cold end of the Talon edge (Run 19). Drive ratio is 6.8%.

in a severe shift in $\langle \dot{h} \rangle_t$ at the 'crevice', however not to such a degree that the time-averaged heat transfer is positive.

The performance deficiency in the 'crevices' of the Talon and Bulbous edge shapes is thought to be due to the induced flow recirculation caused by the enlarged edge shape upstream.

When the prevailing flow is moving rightward, the flow conditions at the left end of the stack for the Talon edge profile are such that a local zone of recirculation forms inside the stack and behind the protrusion, promoting increased contact with the stack plate but also reducing net flow towards the right end of the stack and introducing viscous heating. Heat stored in the protrusion from the phase immediately preceding may then be transferred to cooler gas deep inside the stack which is drawn leftward into the recirculation. This mechanism is believed to exist for even the Rectangular edge shape, where flow over the leading edge creates a similar recirculatory zone, although its impact is less noticeable. This mechanism was not observed with the Rounded stack plate edge shape, suggesting that rounding off the edges of the stack plate will eliminate the described loss mechanism.

3.2. Cooling power

A comparison of the effective cooling power $\dot{Q}_{S,cold}$ of each stack plate edge shape is presented in Fig. 15. This figure shows that only the Rounded edge profile consistently draws greater $\dot{Q}_{S,cold}$ compared to the Rectangular edge shape. Interestingly, all four alternatives considered outperformed the benchmark Rectangular edge shape profile at a drive ratio of 1.7%. However, the performance of the Talon and Bulbous variants underperformed at higher drive ratios when using $\dot{Q}_{S,cold}$ as a performance metric. It can also be seen that the Talon and Bulbous edge shapes require higher acoustic power inputs to achieve the same drive ratio.

Further to the result presented in Fig. 15, the COP of each plate edge shape as defined in Eq. (15) versus drive ratio is presented in Fig. (16). It is quite clear from this figure that the Talon and Bulbous edge shapes are undesirable from an efficiency viewpoint when compared to the

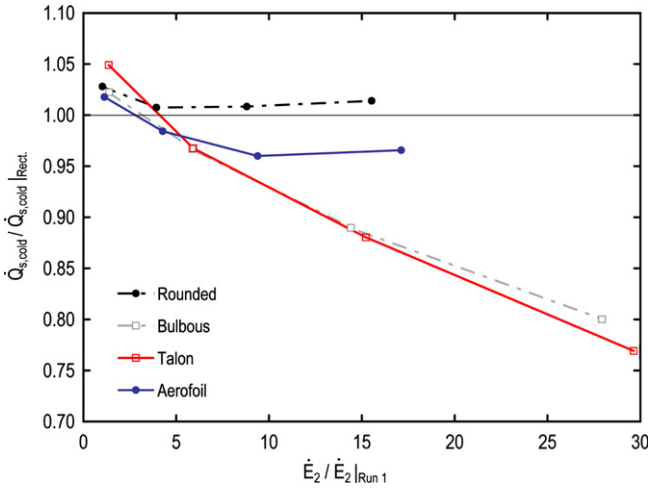

Fig. 15. $\dot{Q}_{S,cold}$ (normalised using rectangular edge shape result) versus $\dot{E}_2$ normalised by the result of Run 1.

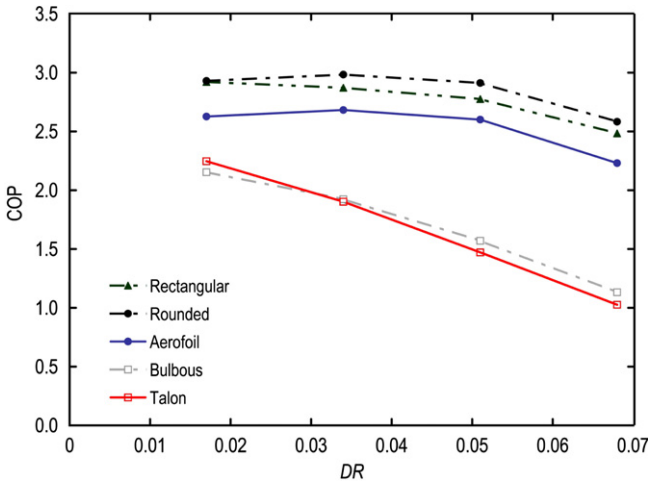

Fig. 16. COP versus drive ratio for all edge shape variants considered in this study.

Rectangular and Rounded edge shapes. The Rounded edge shapes is shown to provide the highest COP of the edge shape variants considered. The Aerofoil edge shapes did not achieve a COP as high as the Rounded or Rectangular edge shapes despite achieving higher $\dot{Q}_{S,cold}$ for a drive ratio of 1.7%.

Note that the COP values presented in this study are a fraction of that expected in practical thermoacoustic systems. The edge shape simulated is at near vacuum ($p_m = 10$ kPa), and the scale of the thermoacoustic couple is much larger (i.e. lower frequency) than that expected in a practical or didactic device.

3.3. Temperature distributions

Fig. 17 presents the gas temperature difference across the thermoacoustic couple, normalised by the gas temperature difference achieved using a rectangular plate, versus

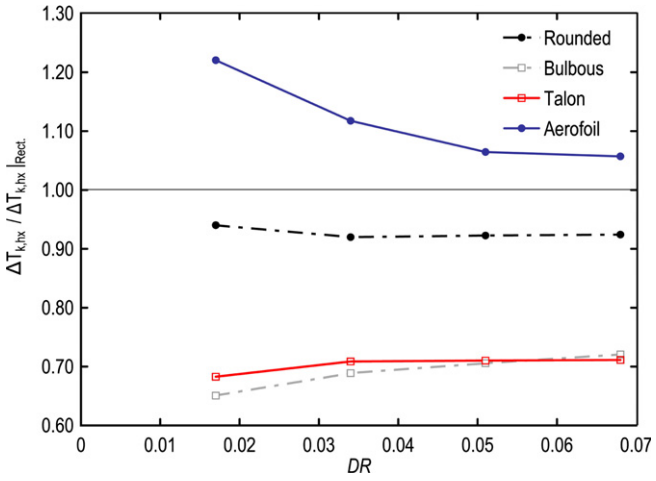

Fig. 17. Normalised $\Delta T_{k,hx}$ versus drive ratio for various edge shapes.

drive ratio and has been normalised by the gas temperature difference achieved using a rectangular plate. This figure shows that for each drive ratio considered, the Aerofoil edge shape is able to generate a higher gas temperature difference between the left and right ends of the plate, $\Delta T_{k,hx}$, than the Rectangular edge shape despite a lower COP, as shown in Fig. 16. Shifting from a rectangular shaped stack plate to a rounded edge plate is expected to result in a $\Delta T_{k,hx}$ reduction of up to 8%, and if using Talon or Bulbous edge shapes, up to 35%.

This result was explored further, on the basis that whilst $\Delta T_{k,hx}$ is a useful measure of performance, it may not include actual temperature extremes if the axial positions at which the minimum and maximum temperatures develop do not correspond with the left and right stack plate edges. It is reasonable to assume that design of thermoacoustic devices involving heat exchangers and a stack will locate the heat exchangers directly up against each end of the stack, and that automatic fine 'tuning' of the axial position of the heat exchangers is unlikely beyond the design phase.

Using a Rectangular edge shape with increasing drive ratio, the time average of gas temperature T_k on the mid-plate spacing centerline ($y = 0$) is presented in Fig. 18. The $\Delta T_{k,hx}$ result is calculated using values obtained on x/L_S equal to 0 and 1, and is considered to be an accurate measure of the gas temperature extremes if the minima and maxima of T_k are obtained on these values of x/L_S. This is observed at most drive ratios simulated, but at a drive ratio of 1.7%, the minimum and maximum values of $\langle T_k \rangle_t$ lie at x/L_S equal to approximately -0.05 and 1.05, respectively, suggesting that $\Delta T_{k,hx}$ understates the performance of the thermoacoustic couple at this drive ratio. Note that as the drive ratio is increased for the Rectangular edge shape, the temperature distribution on $y = 0$ approaches a straight line within the stack (Run 16 shown in Fig. 18).

Fig. 19 shows the distribution of $\langle T_k \rangle_t$ for various edge shapes for a drive ratio of 1.7%. The Talon and Bulbous edge shapes that were identified previously as underper-

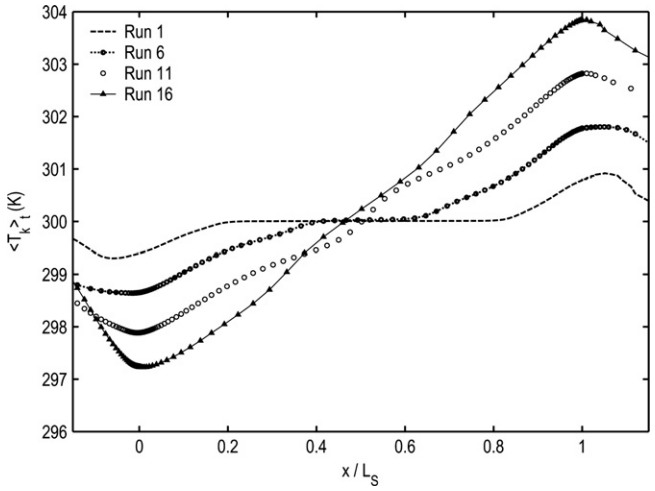

Fig. 18. Time average T_k for the Rectangular edge shape versus axial position normalised by stack length using drive ratios 1.7% (Run 1) to 6.8% (Run 16).

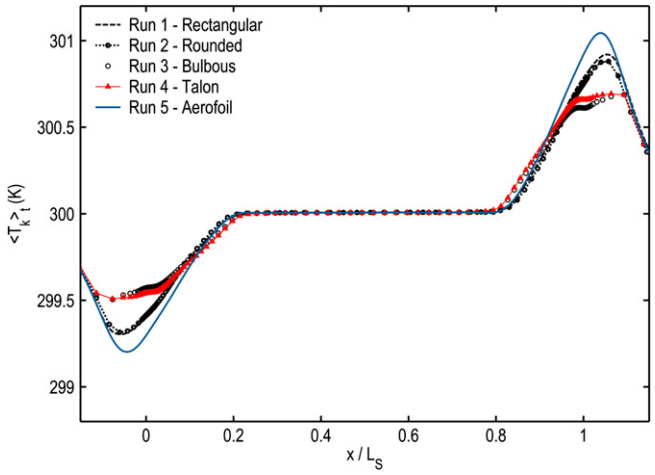

Fig. 19. Time average T_k versus axial position normalised by stack length for selected edge shapes. Runs 1–5 are presented for which the drive ratio is common and equal to 1.7%.

forming, are shown here to again be less effective in establishing a thermal differential between each end of the stack, with a plateau-like shape to the $\langle T_k \rangle_t$ distribution at each end. With the Rectangular and Rounded edge shapes achieving near identical distributions of $\langle T_k \rangle_t$, the Aerofoil edge shape clearly stands out. In Fig. 20, which shows the same comparison except at a higher drive ratio of 5.1%, the trend is continued if one considers the 'cold' end of the device only. The same cannot be said for the right end of the stack at this drive ratio.

At a drive ratio of 5.1%, there are differences in the distribution of the time-averaged gas temperature at the right (hot) end of the stack for the five edge shapes modelled. It is difficult to conclude that one edge shape is more effective at this end than the others, but it may be stated that the maximum value of $\langle T_k \rangle_t$ is achieved by each edge shape at $x/L_S \approx 1$.

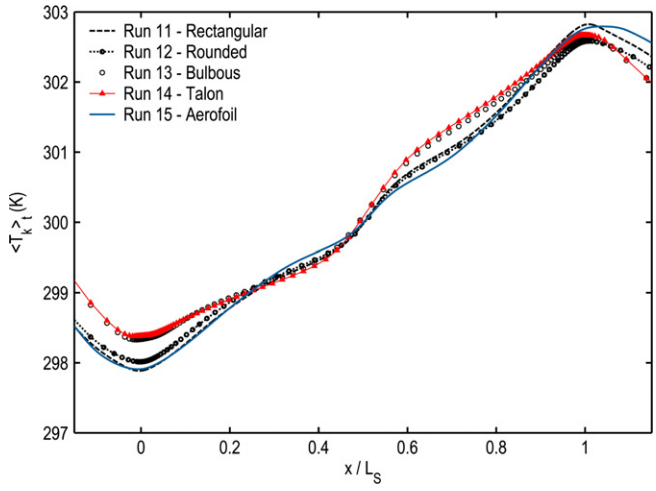

Fig. 20. Time average T_k versus axial position normalised by stack length for selected edge shapes. Runs 11–15 are presented for which the drive ratio is common and equal to 5.1%.

4. Discussion and conclusions

The comparative performance of five thermoacoustic stack plate edge shapes have been estimated using numerical analysis.

The results of the analysis indicate that the thermoacoustic couple edge profile has a significant impact on the overall performance. The influence of stack edge shape upon the flow impedance of the stack is an important consideration when comparing alternative stack edge shapes. The 'sleeker' aerofoil and rounded edge shapes with lower flow resistance are preferable designs, since both the acoustic impedance on the inlet boundary and the effective cooling rate $\dot{Q}_{S,cold}$ were more desirable than other edge shapes considered.

Although the Talon and Bulbous edge shapes are expected to generate a higher rate of heat transfer across the stack face for similar acoustic power inputs at low drive ratios, the same cannot be said for these edge shapes at higher drive ratios. The Talon and Bulbous profiles also do not achieve as high temperature difference, cooling power or efficiency values as the alternative profiles when using the defined parameters $\Delta T_{k,hx}$, $\dot{Q}_{S,cold}$ and COP.

It remains to be seen if stacks with combinations of stack edges (e.g. one edge 'Rounded', the other 'Aerofoil' or 'Rectangular') would have improved performance.

On the basis of the results from this study, rounding the edges of a rectangular stack section is expected to yield improvements in the effective cooling rate and COP. Shifting to an aerofoil-like stack section may not be warranted because of the likely increased complexity and cost of manufacture, despite the predicted increase in $\Delta T_{k,hx}$ over a Rectangular section. The improvement in COP through minimisation of acoustic streaming on the inside face of the stack, and increased $\dot{Q}_{S,cold}$ by greater retention of stack thickness at the plate extremities, leads to recommendation of the Rounded edge shape profile for thermoacoustic stack plates in practical devices.

References

[1] G.W. Swift, Thermoacoustics: a unifying perspective for some engines and refrigerators, Acoust. Soc. Am. (2002).
[2] N. Rott, Thermoacoustics, Adv. Appl. Math. 20 (1980) 135–175.
[3] G.W. Swift, Thermoacoustic engines, J. Acoust. Soc. Am. 84 (1988) 1145–1180.
[4] B. Ward, G.W. Swift, Design Environment for Low-Amplitude Thermoacoustic Engines (DeltaE) Tutorial and User's Guide (Version 5.1), Los Alamos National Laboratory, June 2001.
[5] J. Wheatley, T. Hofler, G.W. Swift, A. Migliori, An intrinsically irreversible thermoacoustic heat engine, J. Acous. Soc. Am. 74 (1) (1983) 153–170.
[6] N. Cao, J. Olsen, G.W. Swift, S. Chen, Energy flux density in a thermoacoustic couple, J. Acous. Soc. Am. 99 (6) (1996) 3456–3464.
[7] G. Mozurkewich, Time-average temperature distribution in a thermoacoustic stack, J. Acoust. Soc. Am. 103 (1) (1998) 380–388.
[8] E. Besnoin, Numerical study of thermoacoustic heat exchangers, Ph.D. Thesis, The Johns Hopkins University, Baltimore, Maryland, 2001.
[9] A.S. Worlikar, O.M. Knio, R. Klein, Numerical simulation of a thermoacoustic refrigerator. II. Stratified flow around the stack, J. Comput. Phys. 144 (1998) 299–324.
[10] H. Ishikawa, D.J. Mee, Numerical investigations of flow and energy fields near a thermoacoustic couple, J. Acous. Soc. Am. 111 (2) (2002) 831–839.
[11] A. Piccolo, G. Pistone, Estimation of heat transfer coefficients in oscillating flows: the thermoacoustic case, Int. J. Heat Mass Transfer 49 (2006) 1631–1642.
[12] L. Zoontjens, C.Q. Howard, A.C. Zander, B.S. Cazzolato, Numerical study of flow and energy fields in thermoacoustic couples of non-zero thickness, Int. J. Therm. Sci., submitted for publication.
[13] Fluent Inc., FLUENT 6.2.16 User Manual, Lebanon, NH, USA, 2006.
[14] A. Mills, Heat Transfer, second ed., Prentice Hall, NJ, USA, 1999.